Materials Science & Engineering A 706 (2017) 287–294

Contents lists available at ScienceDirect

Materials Science & Engineering A

journal homepage: www.elsevier.com/locate/msea

Quantitative relationship between anisotropic strain to failure and grain morphology in additively manufactured Ti-6Al-4V

Alexander E. Wilson-Heid, Zhuqing Wang, Brenna McCornac, Allison M. Beese*

Department of Materials Science and Engineering, Pennsylvania State University, University Park, PA 16802, USA

ARTICLE INFO

Keywords:
Powder bed fusion
Additive manufacturing
Ti-6Al-4V
Pulsed laser
Continuous-wave laser
Anisotropic ductility

ABSTRACT

The aim of this study was to identify processing-microstructure-mechanical property links in additively manufactured Ti-6Al-4V. First, the microstructure and mechanical properties of Ti-6Al-4V produced via two laser powder bed fusion (LPBF) additive manufacturing (AM) methods, one using a pulsed laser (P-LPBF) and the other a continuous-wave laser (CW-LPBF), were investigated and compared. Second, existing data from the literature were integrated with the present data in order to identify a general quantitative relationship between anisotropic ductility and grain morphology in additively manufactured Ti-6Al-4V. This revealed that an exponential relationship exists between the anisotropic grain morphology and anisotropic elongation to failure in Ti-6Al-4V. In particular, this relationship shows that a prior-β grain aspect ratio (grain height to grain width) exceeding 6 results in significant anisotropy in elongation. Namely, the columnar grains dominate the fracture mechanics by furnishing significant damage accumulation paths for tension in the longitudinal direction, resulting in higher ductility in the build direction than that in the longitudinal direction. With respect to processing, it was shown that as-built CW-LPBF samples had nearly equiaxed grains while those made by P-LPBF had elongated columnar grains. This resulted in greater yield strength, ultimate tensile strength, and ductility in the CW-LPBF samples compared to P-LPBF samples.

1. Introduction

Powder bed fusion (PBF) additive manufacturing (AM) of metals uses a laser or electron beam to selectively melt powder metal feedstock to build 3-dimensional (3D) components in a layer-by-layer fashion [1]. This process allows for the production of custom, complex, and near-net-shape components [2]. In PBF, a layer of metal powder is spread across a substrate or previous layer, and a laser or electron beam scans the pattern of the current layer, selectively melting the powder to complete the 2-dimensional layer. As the heat source scans across the powder, the melt pool cools, and the cooled metal fuses to the substrate or layer below. Once a layer is complete, the substrate is lowered, another layer of powder is added, and the process is repeated until the part is complete [3]. The final part is then extracted from the surrounding un-melted powder.

During processing, the thermal gradient between the melt pool and previously solidified layers, which depends on processing parameters, geometry of the component, and location within the component, results in a location-dependent thermal history throughout the component [4]. The rapid heating, solidification, and cooling of the material dictates the growth direction and morphology of the grains, resulting in heterogeneous and anisotropic microstructures [5].

Laser based PBF systems use either continuous-wave (CW) laser emission [6–10] or power modulated “pulsed” fiber laser emission [10–12] as the heat source for selectively melting the powder metal feedstock (referred to throughout as CW-LPBF and P-LPBF, respectively). A CW laser produces a continuous, uninterrupted beam of light with a constant output power, while pulsed fiber lasers in PBF are power modulated to generate pulsed (e.g., a square wave) patterns as a function of time [13].

Previous research has been performed to investigate the mechanical properties of additively manufactured Ti-6Al-4V in the build (transverse) and longitudinal directions. These studies have shown that the strength in as-built samples is nearly isotropic, while the elongation to failure is higher in the transverse direction than the longitudinal direction [14–21]. This trend in ductility is reversed for samples in which significant porosity is identified, when the internal defects, rather than grain structure, drive the anisotropic ductility [22,23].

The present work focuses on identifying quantitative links between the anisotropy in ductility and the microstructure in additively manufactured Ti-6Al-4V. The microstructure, namely the prior-β grain morphology, and tensile mechanical properties of samples fabricated using

* Corresponding author.
E-mail address: amb961@psu.edu (A.M. Beese).

http://dx.doi.org/10.1016/j.msea.2017.09.017
Received 12 July 2017; Received in revised form 2 September 2017; Accepted 5 September 2017
Available online 06 September 2017

CW-LPBF and P-LPBF were investigated. Additionally, studies from literature were analyzed to quantify grain morphology and its impact on anisotropic ductility. From these data, a quantitative correlation describing anisotropic tensile ductility based on grain morphology is developed. Additionally, this study presents the effect of processing conditions on the microstructure and tensile mechanical properties of Ti-6Al-4V fabricated via CW-LPBF and P-LPBF. The effect of microstructure (CW versus pulsed), direction (anisotropic microstructure in CW versus pulsed), and surface roughness (macroscopic structure in P-LPBF) on properties was investigated.

2. Experimental

2.1. Fabrication

To identify the difference of the impact of CW laser versus a pulsed laser processing in PBF on microstructure and properties, Ti-6Al-4V samples were fabricated using both of these laser heat sources. For CW-LPBF (EOSINT M280), 32 mm × 30 mm × 4 mm walls were fabricated on a 280 mm × 280 mm annealed Ti-6Al-4V substrate in an Ar filled chamber to minimize oxygen contamination. Samples were fabricated using the CW laser parameters in Table 1. Prior to sample removal from the substrate, the entire build was subjected to a standard PBF stress relief in Ar at 650 °C for 3 h. Uniaxial tension samples were extracted from the deposited walls in the horizontal (longitudinal) and vertical (transverse) directions using wire electrical discharge machining (EDM). The tensile sample geometry used was in accordance with ASTM E8 [24], with a gauge length of 6 mm and cross sectional area of 1.5 mm^2 as shown in Fig. 1a.

Conversely, samples made using P-LPBF (Renishaw AM 250) were fabricated directly in the uniaxial tension sample geometry shown in Fig. 1b, which was also in accordance with ASTM E8, with a gauge length of 21.3 mm and a cross sectional area of 8 mm^2. Samples were fabricated in two orientations, transverse and longitudinal, on a 250 mm × 250 mm substrate in an Ar filled chamber with the baseplate heated to 170 °C throughout the build process. The fabrication parameters used for the near-net-shaped P-LPBF samples are specified in Table 1. Although there was a smaller gauge region in the CW-LPBF samples, the sample dimensions incorporated the same order of magnitude of grains for mechanical testing to be representative of bulk properties. For P-LPBF samples, ten samples were fabricated such that their tensile axes were in the transverse direction, and ten were fabricated such that their tensile axes were in the longitudinal direction. The grips of the longitudinal samples were fabricated directly on the substrate, while support structure was used in the gauge region to maintain sample geometry during fabrication. Prior to sample removal from the substrate, the entire build was subjected to the same stress relief heat treatment as the CW-LPBF samples. Samples were removed from the substrate using wire-EDM, and subjected to a grit blasting to remove un-melted powder. Half of the samples in each orientation were left in this as-built condition for tensile testing, while the gauge regions of the other half of the samples were milled to determine how the surface finish impacted the measured properties.

Table 1
Processing parameters used for manufacturing samples via CW-LPBF and P-LPBF.

	Continuous-wave laser	Pulsed laser
Substrate temperature (°C)	25	170
Laser power (W)	340	188
Scanning speed (mm/s)	1250	1000
Hatch spacing (μm)	140	100
Layer height (μm)	60	30
Laser spot size (μm)	70–80	70

2.2. Mechanical testing

To quantify the mechanical properties that result from CW-LPBF versus P-LPBF processing, samples from each build were subjected to tensile testing. Uniaxial tensile testing of the P-LPBF samples was performed on an electromechanical testing frame (Instron 4202) with a 10 kN load cell (Instron model 2518-804). Uniaxial tension testing of the smaller CW-LPBF samples was performed on a servo-hydraulic load frame (810 MTS) with a 25 kN load cell (MTS model 661 20E-01). All tensile tests were performed under quasi-static conditions with a strain rate on the order of 10^{-4} s^{-1}. Digital image correlation (DIC), a non-contact method for measuring surface deformations, was used to compute surface strains using correlation software (Vic2D, Correlated Solutions). Sample gauge regions were painted with a white basecoat followed by a random black speckled pattern on top. A digital camera (Point Grey GRAS-50S5M-C) was used to take images of the deforming gauge region of the sample at 1 Hz during each test. The surface deformations in the gauge region of each sample were computed from the digital images using a cubic B-spline interpolation algorithm with a subset size of 21 pixels and a step size of 5 pixels. The axial strain in the gauge section of each sample was measured using a vertical virtual extensometer measuring 5.5 mm for the CW-LPBF samples and 20 mm for the P-LPBF samples.

Microhardness was measured using a Vickers indenter (Leco MHT Series 200) with a load of 300 g and a dwell time of 15 s. At least nine locations at varying distances from the substrate were analyzed for microhardness, with five indentations at each height, in both P-LPBF and CW-LPBF samples.

2.3. Sample characterization

X-ray computed tomography (CT), a non-destructive measurement technique, was used to visualize internal porosity. For this study, X-ray CT (General Electric phoenix v|tome|x m) was used to identify any lack-of-fusion porosity in two samples, one from each orientation, made by P-LPBF and a wall from which the CW-LPBF samples were extracted. Scans were performed using a 300 kV micro-focus X-ray source with a GE DXR250 flat panel detector with a 200 mm pitch. An accelerating voltage of 200 kV, a tube current of 125 μA, and a voxel size of 20 μm were used with 950 projections per scan. This voxel size allows for the identification of pores 40–60 μm in diameter or larger [25,26]. The scans were analyzed using VGStudio Max 2.2 visualization and analysis software to identify pore morphology.

The Archimedes method for determining density was used to quantify porosity. The sample density was computed as:

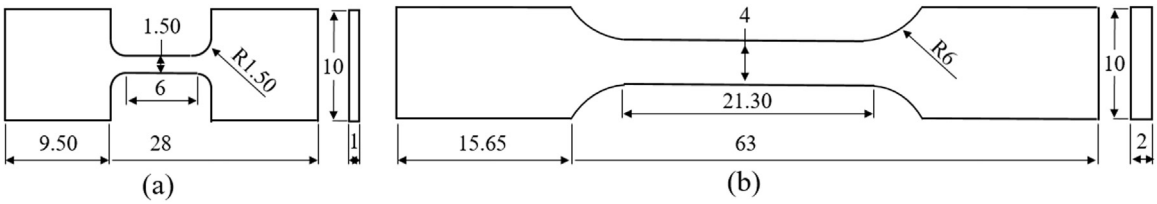

Fig. 1. Geometries of tensile samples (a) extracted from walls made using CW-LPBF (EOSINT M280), and (b) directly built using P-LPBF (Renishaw AM250). Dimensions are in mm.

$$\rho = \left(\frac{M_a}{M_a - M_w}\right)\rho_w \quad (1)$$

where M_a is the measured mass of the sample in air, M_w is the measured mass of the sample in water, and ρ_w is the density of water, which was assumed to be 1.0 g/cm^3. Calculated densities were compared with the theoretical density of Ti-6Al-4V, 4.43 g/cm^3 [27], to determine the percent density in the analyzed samples.

For microstructural analysis, samples were prepared using standard metallurgical procedures with a final polish using 0.05 μm colloidal silica, and etched using Kroll's reagent (2 vol% hydrofluoric acid and 3 vol% nitric acid in distilled water). Images of the microstructures were taken using a digital optical microscope (OM, Keyence VHX-2000). The digital OM was also used for 3D surface reconstruction of the samples for surface roughness analysis.

To quantify the grain dimensions in the present study and from reported data, selected micrographs were overlaid with a five by five grid pattern aligning with the longitudinal and transverse directions. Grain dimensions were computed based on how many grain boundaries each line intersected. Due to the elongated morphology of grains, the line lengths were dictated by grain boundary locations, so that a line started on a grain boundary and ended on another. Measurements were made for each individual line three times for a total of fifteen measurements in each orientation. To ensure proper statistics of measurements, this procedure was repeated for each micrograph by five individuals. The twenty-five grain dimensions per orientation were used to determine the average width/height of the grains for each micrograph.

3. Results and discussion

3.1. Overview: continuous-wave versus pulsed laser

The measured mechanical properties for all samples are given in Table 2, and representative engineering stress-strain curves of CW-LPBF, as-deposited P-LPBF, and machined P-LPBF samples under uniaxial tension are shown in Fig. 2. The variations in both ultimate tensile strength (UTS) and elongation to failure indicate that differences in processing conditions and surface finish influenced the bulk material properties. In general, the CW-LPBF samples had higher yield strength (0.2% offset), UTS, and elongation to failure in both orientations tested compared to the corresponding machined P-LPBF samples. In the same direction, CW-LPBF samples had higher elongations than the as-built and machined P-LPBF samples. The average yield strength of CW-LPBF samples was 8.3% higher, and the average UTS 6.7% higher, than that of the machined P-LPBF samples.

Microhardness as a function of vertical position from the substrate was measured to determine if the mechanical properties, and indirectly, microstructure, had a location dependence that would impact the properties within the gauge regions of the samples. In the CW-LPBF samples, the centers of the gauge region for the longitudinal samples and transverse samples were approximately 5 mm and 13 mm from the baseplate, respectively, and microhardness measurements were taken at heights from 3 mm to 24 mm from the baseplate. In P-LPBF samples, the center of the gauge region for the longitudinal and transverse samples was approximately 5 mm and 32 mm away from the baseplate, respectively, and microhardness measurements were taken at heights from 1 mm to 9 mm away from the baseplate. As shown in Fig. 3, the microhardness as a function of distance from the substrate was found to be constant by the time the gauge region was reached in all samples. Thus, the gauge regions are sufficiently far from the baseplate such that the microstructure has reached a steady state in all of the tested samples.

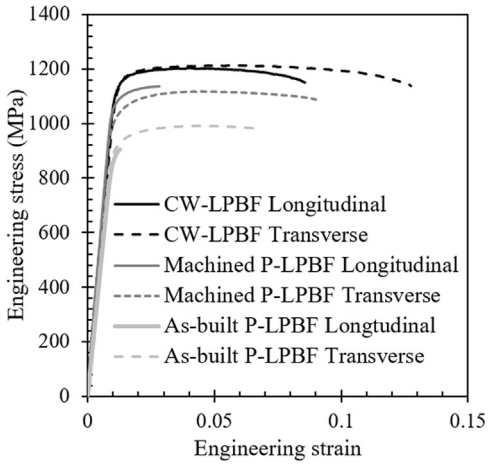

Fig. 2. Representative engineering stress-strain curves for samples fabricated using CW-LPBF and P-LPBF in two orientations, showing little anisotropy in strength in the CW-LPBF samples, and a higher strength in the longitudinal direction than the transverse direction in P-LPBF samples. With both processing conditions, samples in the longitudinal direction had lower ductility than those in the transverse direction; however, this difference is more dramatic in the P-LPBF samples.

The average hardness in the CW-LPBF samples was 403 ± 8 HV compared to 375 ± 7 HV in the P-LPBF samples. These values agree with existing literature, for which the hardness of Ti-6Al-4V fabricated by PBF has been reported to be greater than traditionally processed Ti-6Al-4V (341–369 HV) [2,5,28,29].

X-ray CT scans revealed that neither CW-LPBF nor P-LPBF samples contained lack-of-fusion porosity. The representative as-built longitudinal and transverse P-LPBF samples examined with the Archimedes method showed that the samples were 99.7 ± 1.3% and 98.7 ± 2.2% dense, respectively. The CW-LPBF deposited wall had a density of 98.2 ± 1.9% measured via Archimedes method. These analyses indicate samples were near fully dense with only gaseous, spherical porosity present.

Table 2
Comparison of tensile mechanical properties for samples made with CW-LPBF and P-LPBF lasers, where n indicates the number of samples tested in each condition. Values reported are average ± standard deviation.

		n	**Modulus**(GPa)	**Yield strength** (MPa)	**Ultimate tensile strength** (MPa)	**Elongation** (%)
Continuous-wave laser	Longitudinal	16	103 ± 2.0	1137 ± 10.3	1204 ± 13.0	8.5 ± 1.1
	Transverse	3	103 ± 2.4	1141 ± 1.5	1207 ± 6.7	12.7 ± 1.1
Pulsed laser	Longitudinal, as-built	3	93 ± 0.9	893 ± 5.8	912 ± 5.9	1.4 ± 0.2
	Longitudinal, as-built, area corrected for E = 110 GPa	3	110	1060 ± 10.0	1082 ± 15.9	
	Longitudinal, machined	3	110 ± 5.6	1078 ± 2.9	1131 ± 17.4	2.8 ± 0.8
	Transverse, as-built	4	95 ± 1.7	916 ± 4.8	992 ± 5.9	6.5 ± 1.0
	Transverse, as-built, area corrected for E=110 GPa	4	110	1060 ± 18.3	1149 ± 15.4	
	Transverse, machined	3	110 ± 4.6	1010 ± 0.0	1117 ± 1.2	7.8 ± 1.1

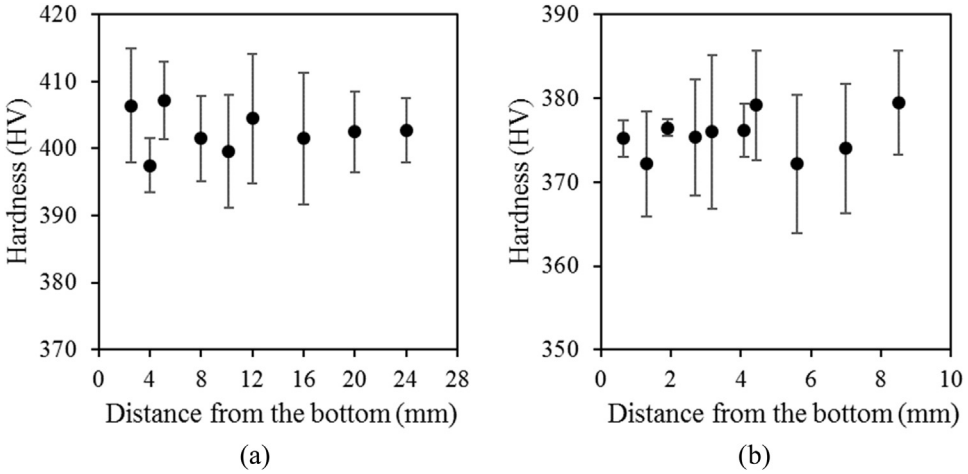

Fig. 3. Hardness as a function of position for the (a) CW-LPBF samples and (b) P-LPBF samples. Both plots show little variation in microhardness as a function of distance from the substrate, indicating that a steady-state hardness regime has been reached throughout the samples.

3.2. Anisotropy

The tensile mechanical properties of samples were measured in the longitudinal and transverse orientations with respect to the build layers to determine the degree of anisotropy of components made by PBF. As shown in Table 2, samples fabricated via CW-LPBF exhibited isotropic yield strength and UTS, but anisotropic strain to failure, with a higher elongation in the transverse direction. Near isotropic yield strength and UTS behavior was observed in the milled P-LPBF samples, and similar to CW-LPBF samples, the elongation in the milled P-LPBF samples was higher in the transverse direction than in the longitudinal direction.

The isotropic strength behavior in both sets of samples can be explained by the low strain hardening behavior in Ti-6Al-4V [30]. The tensile stress versus plastic strain curve can be fit with a power law (e.g., [31]) equation, given as:

$$\sigma = k\varepsilon_P^n \tag{2}$$

where σ is the true stress, ε_p is the plastic strain, k is the strength coefficient, and n is the strain hardening exponent. The strain hardening exponents for CW-LPBF and P-LPBF samples were found to be 0.06 and 0.08, respectively. The very low strain hardening rate in both sets of

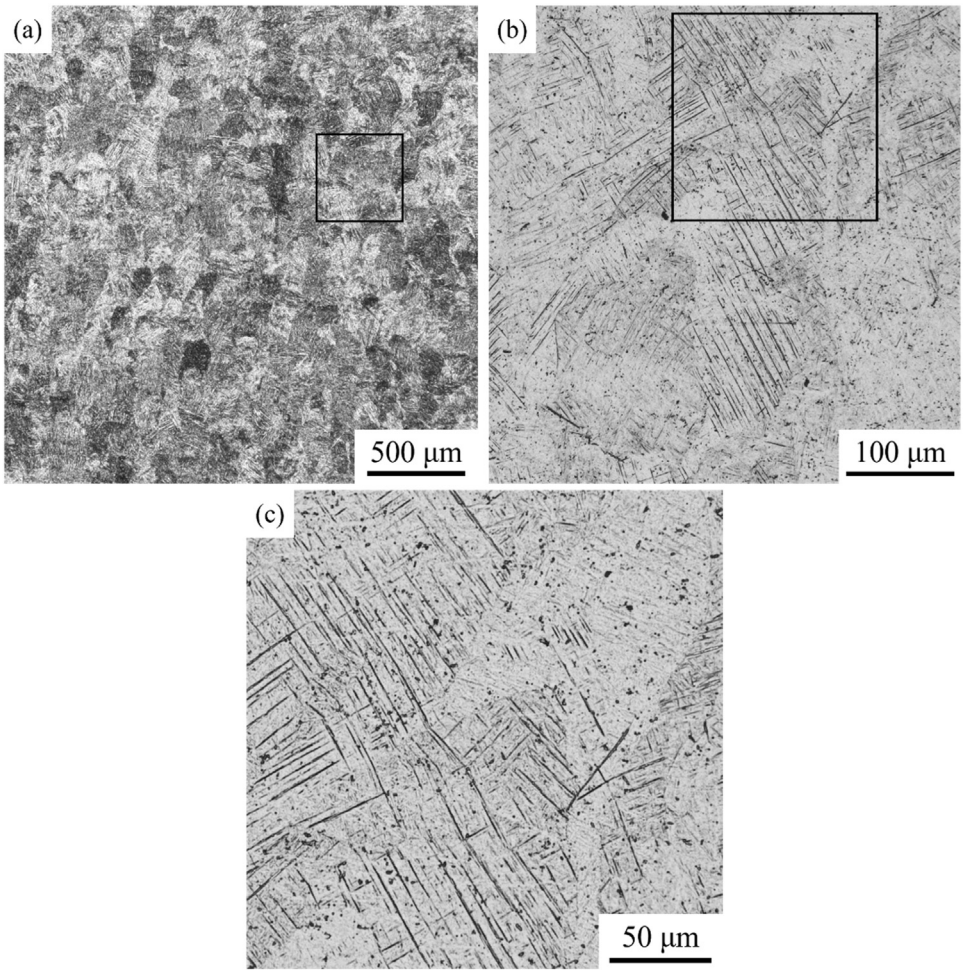

Fig. 4. Optical micrographs of a CW-LPBF Ti-6Al-4V sample, in which build direction is vertical, showing (a) the equiaxed prior-β grain morphology; (b) an enlarged image of the inset in (a) showing prior-β grains in more detail and α-laths within the prior-β grains; and (c) an enlarged image of the inset in (b) showing the acicular α-lath morphology.

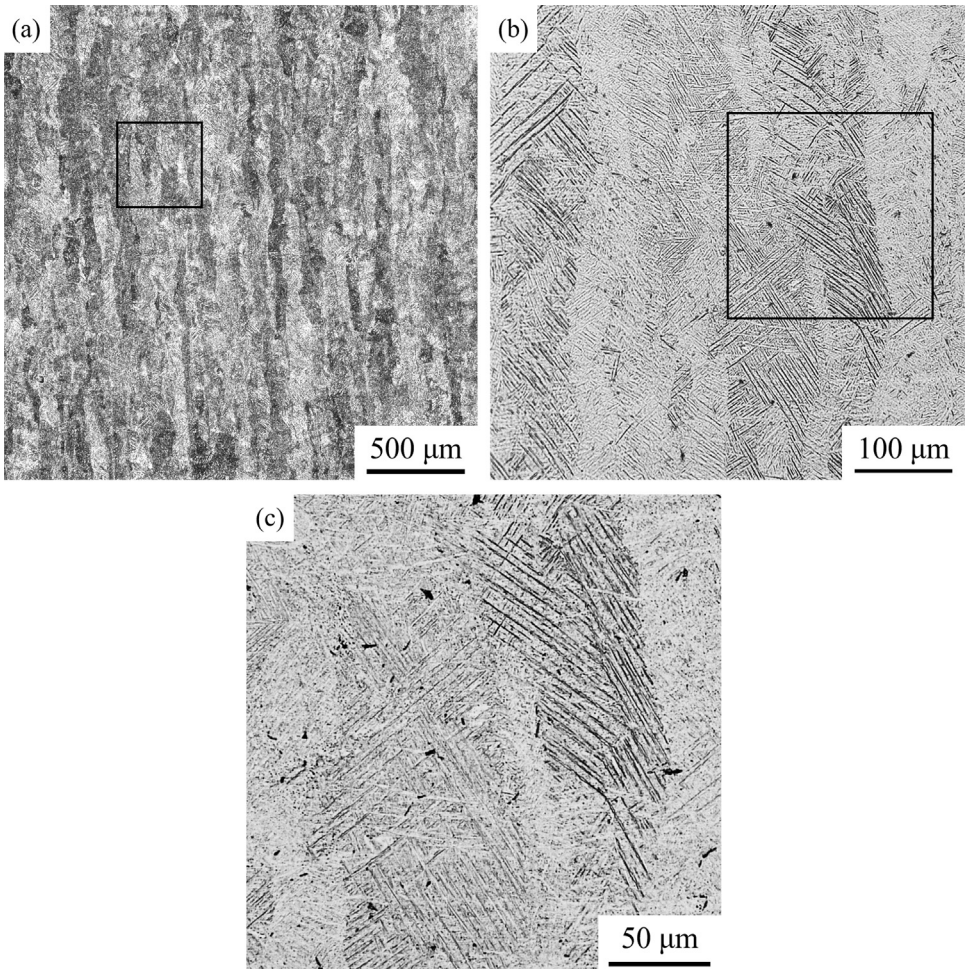

Fig. 5. Optical micrographs of a P-LPBF Ti-6Al-4V sample, in which build direction is vertical, showing (a) the elongated prior-β grain morphology; (b) an enlarged image of the inset in (a) showing prior-β grains in more detail and α-laths within the prior-β grains; and (c) an enlarged image of the inset in (b) showing the acicular α-lath morphology.

samples, in which the yield strength was isotropic, resulted in isotropic UTS despite anisotropy in elongation to failure. We note that although the prior-β grain morphologies differ, which impacts elongation, as discussed in Section 3.3, the plasticity behavior in Ti-6Al-4V is dictated by the α lath morphology and preferred orientation [19], neither of which varied within each sample set, as shown in Figs. 4 and 5.

3.3. Effect of processing on microstructure

To explain the differences in the mechanical properties of Ti-6Al-4V samples manufactured using CW or pulsed lasers, the microstructures were analyzed, and the prior-β grain dimensions were quantified. Prior-β grains that grow epitaxially across several build layers in AM have been widely reported in literature [4,16,18,19,32–35]. The microstructures in the CW-LPBF and P-LPBF samples are shown in Figs. 4 and 5, respectively. There is a clear difference in prior-β grain size and morphology between the two processing methods. The microstructure of the sample made via CW-LPBF (Fig. 4) contains small, nearly equiaxed prior-β grains, with average measured widths of 96.3 ± 18.0 μm and lengths (in the build direction) of 125.3 ± 14.4 μm, and the prior-β grains contain acicular α laths. The samples made with P-LPBF (Fig. 5) also have prior-β grains containing acicular α-laths; however, the prior-β grains are elongated and extend across multiple build layers, with the measured dimensions of 150.3 ± 22.7 μm wide by 1201.8 ± 190.2 μm long.

In welding research, it has been shown that the morphology and size of grains are controlled by the relationships between thermal gradient (G) and the solidification growth rate (R) of as-deposited material [36]. The ratio G/R influences grain morphology, where a low value results in the formation of equiaxed grains, which transition to columnar grains with increasing G/R values. The product GR, or the solidification cooling rate, controls the size of the grain structure, with higher values resulting in smaller grains. These relationships have also been noted in AM simulations and experiments [37–39]. The microstructural variations between the two processing methods in the current study can be explained by relating the input parameters and the knowledge of thermal behavior in AM to G and R.

In CW-LPBF, with increasing scanning speed, the melt pool becomes elongated behind the laser spot, resulting in a decreasing thermal gradient, increasing solidification growth velocity at the melt pool boundary, and decreasing G/R ratio [37,40]. This results in fine, equiaxed grains, as shown in in Fig. 4 for the CW-LPBF build.

The laser in P-LPBF build does not simultaneously supply energy to the build and vary position, but rather supplies bursts of power at discrete locations. This results in a higher thermal gradient at the boundary of the melt pool compared to a continuously scanning laser, and is similar to spot welding [41]. Therefore, the solidification growth velocity in P-LPBF is not influenced by the scanning speed of the laser, rather it is driven by the cooling rate. In a prior study of pulsed versus continuous-wave laser processing, for an equivalent thermal gradient, the cooling rate in P-LPBF of AlSi10Mg was found to be orders of magnitude higher (1.1×10^5 K/s) than that in CW-LPBF (4.0×10^3–1.0×10^4 K/s) [42]. The P-LPBF parameters used in the present study resulted in a fine, columnar structure (Fig. 5), which has also been observed in other studies for builds with large G/R ratios [39,43].

Table 3
Grain aspect ratio (grain height/grain width) and elongation ratio (transverse elongation/longitudinal elongation) for tests performed in the present study as well as data from literature for both powder bed fusion and directed energy deposition (DED) AM. Values reported are average ± standard deviation.

Grain aspect ratio	Elongation ratio	AM system	References
1.20 ± 0.42	1.00 ± 0.21	Realizer SLM100	[16]
1.30 ± 0.29	1.49 ± 0.23	EOSINT M280	Present study, CW-LPBF
2.38 ± 0.65	1.06 ± 0.34	Custom DED	[47]
4.77 ± 0.86	1.05 ± 0.00	EOS M270	[34]
5.22 ± 1.18	0.98 ± 0.17	EOS M270	[33]
5.30 ± 1.82	0.98 ± 0.15	EOS M270	[4]
5.79 ± 0.90	1.32 ± 0.19	Custom DED	[19]
6.71 ± 1.60	1.55 ± 0.39	Concept LaserM2 Cusing SLM	[20]
8.00 ± 1.75	2.79 ± 0.89	Renishaw AM250	Present study, P-LPBF

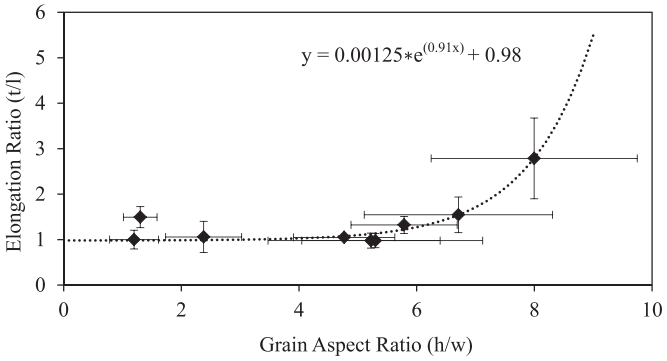

Fig. 6. Elongation ratio (transverse elongation, t/longitudinal elongation, l) versus grain aspect ratio (grain height, h/grain width, w) for tests performed in the present study as well as data from literature [4,16,19,32–34,47]. These data show that as the grain aspect ratio increases above 6, the elongation ratio, and therefore anisotropy in ductility, increases substantially.

3.4. Quantitative relationship between microstructure and anisotropic ductility

To quantitatively compare the two microstructures, the grain aspect ratio, or grain height divided by grain width, was computed for CW-LPBF and P-LPBF samples, as well as microstructures in prior literature, as tabulated in Table 3. In the CW-LPBF samples, this aspect ratio was 1.3, indicating nearly equiaxed grains, while grains in the P-LPBF samples had a much higher aspect ratio of 8.0. This significant difference is attributed to the disparate thermal histories of these samples, which were dictated by different energy inputs, different scanning approaches, and different thermal conditions during fabrication, as described in Section 3.3.

Carroll et al. found that prior-β grain boundaries, which contain semi-continuous α phase, act as damage accumulation sites under load [19]. The α phase is less ductile than the β phase [44]. When tension is applied to separate prior-β grains, therefore subjecting the grain boundary α to tension, these grain boundaries act as damage accumulation pathways. Therefore, the presence of high aspect ratio prior-β grains, which present long, continuous grain boundaries in the build direction, results in a lower strain to failure in longitudinal samples, than transverse samples as described in more detail in [19].

We propose using the grain morphology to describe, and potentially predict, anisotropic elongation behavior in Ti-6Al-4V. To elucidate any quantitative links between the anisotropic microstructure and the anisotropic ductility in Ti-6Al-4V made by AM, the elongation to failure ratio, defined as the strain to failure in the transverse direction divided by that in the longitudinal direction, versus the grain aspect ratio, is plotted in Fig. 6 and tabulated in Table 3, for data reported in the literature and the present study. Each data point included comes from a study that reported elongation in the transverse and longitudinal directions as well as a micrograph showing complete prior-β grains. Studies in which the grain lengths were not fully encompassed in the micrographs were not included, as the grain dimensions could not be fully quantified. Additionally, in order to isolate the effect of grain morphology only, data for which the elongation in the transverse direction was less than that in the longitudinal direction, resulting in an elongation ratio less than 1, were excluded due to presumed or identified internal defects. In a fully-dense Ti-6Al-4V component, where grains grow vertically across build layers, the elongation in the transverse direction should be greater than that in the longitudinal direction due to the preferential damage accumulation along prior-β grain boundaries [19]. However, sharp lack-of-fusion (LOF) porosity, which is commonly present in additively manufactured components, can result in samples having an elongation ratio of less than 1 [22]. LOF pores have long axes perpendicular to the build direction, and act as stress risers when tension is applied in the transverse direction; thus, these internal defects limit ductility in the transverse direction, resulting in an elongation ratio of less than 1. Since the focus of the present study is on linking the grain morphology to ductility, these data were excluded.

The data of anisotropic elongation versus grain aspect ratio in Fig. 6 were fitted with an exponential curve passing through the point (1.0, 1.0), corresponding to an isotropic sample. This resulted in the following empirical description of the elongation ratio (y) as a function of grain aspect ratio (x):

$$y = 0.00125e^{0.91x} + 0.98 \quad (3)$$

This expression can be used to describe and predict the strain to failure ratio between two directions in additively manufactured Ti-6Al-4V based only on the prior-β grain aspect ratio. These data show that grain aspect ratios below about 6 do not lead to significant anisotropy in elongation, as there is enough of a distribution in grain sizes in those samples to dilute the impact of anisotropic grains. However, once the grain aspect ratio exceeds 6, the anisotropy in elongation becomes significant as the elongated grains dominate the mechanics by furnishing significant damage accumulation paths when tension is applied in the longitudinal direction.

With respect to the present samples, when the P-LPBF samples are loaded in tension along the longitudinal direction, the grains are perpendicular to the loading axis, and are separated by grain boundaries, composed of grain-boundary α. Therefore, the grains are pulled apart in Mode I fracture opening fashion [19]. However, when applying tension along the transverse or build direction, the tension acts parallel to the long, continuous prior-β grain boundaries. This results in higher damage accumulation and reduced elongation to failure in the longitudinal compared to transverse samples. Conversely, in the CW-LPBF samples, the nearly equiaxed prior-β grains do not provide for higher damage accumulation in one direction compared to another, resulting in nearly isotropic elongation behavior.

3.5. Effect of surface roughness on properties

As noted in prior literature, surface roughness of as-built samples, due to both the layered fabrication process as well as partially melted particles adhered to sample surfaces, can result in an overall decrease in the elongation to failure of the material [15,45,46]. The rough surface of as-built samples provides stress concentration sites under loading, which can lead to crack nucleation and early failure. This is particularly apparent when tension is applied in the transverse direction, as the sharp surface features, corresponding to subsequent layers, are subjected to Mode I opening loading. Conversely, the build layers in samples built in the longitudinal direction align with the tensile axis of these samples; thus, the ductility in these samples is not as significantly impacted by these features.

Here, the effect of surface finish was examined for the P-LPBF

Table 4
Surface roughness (R_a) measurements of the pulsed laser samples in the as-built and machined conditions. Measurements taken in the gauge region. Values reported are average ± standard deviation.

	Surface roughness, R_a (μm)
As-built transverse	33.90 ± 5.51
As-built longitudinal top surface	22.25 ± 5.58
As-built longitudinal bottom surface (support structure edge)	144.31 ± 13.54
Machined (milled) longitudinal	20.71 ± 3.50
Typical range for milled condition [48]	0.20–25
Typical range for wire EDM condition [48]	0.80–12.5

samples. The layer stepping effect was noticeable on the surface of these as-built samples, and the impact of surface finish on properties is seen when comparing the elongation of the as-built and machined P-LPBF samples in Table 2. The transverse as-built samples had an elongation of 6.5 ± 1.0%, which increased to 7.8 ± 1.1% upon milling. Surface roughness was also apparent in the longitudinal P-LPBF samples due to necessity of incorporating support structures for their fabrication, and as such, the elongation to failure increased in these samples from 1.4 ± 0.2% to 2.8 ± 0.8% upon surface machining.

A quantitative assessment of the surface roughness was made by analyzing surface line profiles generated from OM 3D reconstruction images taken on the thin edge of the gauge region of the P-LPBF tensile samples, as shown in Table 4. The data show that milling reduced surface roughness (R_a) from 33.90 ± 5.51 μm to 20.71 ± 3.50 μm for the transverse samples. Milling was most effective for the longitudinal samples that were built with support structure, reducing the R_a value from 144.31 ± 13.54 μm to 20.71 ± 3.50 μm. As milling removed the stress concentrations due to surface roughness, the elongation increased.

Additionally, undulations in the cross-sectional area due to the layer-by-layer fabrication process, as well as partially melted particles on the surface, of as-built samples result in the overestimation of continuous load bearing cross-sectional area, and therefore, the underestimation of the sample strength [1]. To compare properties of samples with as-built surfaces to those reported with machined surfaces, both of which are presented in disparate studies in the literature, a correction technique is needed. In the present study, the cross-sectional area for each rough as-built P-LPBF sample was originally measured using calipers to measure width and thickness of the gauge region. Due to the nearly fully dense samples verified by X-ray CT, the elastic modulus of as-built Ti-6Al-4V samples should have been equivalent to the milled samples, which was measured to be 110 GPa. To correct for the surface roughness and estimate the load-bearing yield and ultimate tensile strengths of the as-built samples, load-bearing cross-sectional areas were computed to be those that reproduced the expected elastic modulus of 110 GPa for each of the as-built samples. With these load-bearing cross-sectional areas, the yield and ultimate tensile strengths were recalculated. This correction resulted in strengths comparable to the milled samples for both orientations as shown in Table 2. This correction technique may be used for computing representative strength values for as-built samples, or for comparing strength data among studies in the literature with disparate surface finishes.

4. Summary and conclusions

In the present paper, the anisotropic microstructure in additively manufactured Ti-6Al-4V was quantitatively linked to the anisotropic ductility using samples manufactured with a continuous-wave laser PBF system, a pulsed laser PBF system, and data from literature. Additionally, a method for comparing strengths measured for samples with different surface roughness conditions was presented. The following primary conclusions can be drawn from this study:

- For fully dense, near defect-free Ti-6Al-4V fabricated using AM, the elongation to failure was determined to be anisotropic with prior-β grain aspect ratios greater than 6. In these samples, the elongation was higher in the transverse direction than longitudinal direction. The quantitative relationship proposed herein to link microstructure to anisotropic elongation can be used to predict the anisotropic elongation to failure behavior in additively manufactured Ti-6Al-4V with knowledge of only prior-β grain morphology.
- The variations in AM processing conditions studied here resulted in variations in grain morphology, and consequently mechanical properties. The P-LPBF samples contained prior-β grains with a high aspect ratio induced by a high G/R ratio. This led to anisotropic elongation. The CW-LPBF samples had nearly equiaxed grains due to a low G/R ratio, resulting in nearly isotropic elongation behavior.
- The finer grains in the CW-LPBF samples compared to the P-LPBF samples resulted in higher ultimate tensile strength, yield strength, and elongation in the CW-LPBF samples.
- Correcting for surface roughness in as-built P-LPBF samples through calculation of a representative load-bearing cross-sectional area can be used to compare strengths of as-built samples with rough surfaces to those of samples with machined surfaces reported in the literature.

Acknowledgments

The financial support provided by the National Science Foundation through award numbers CMMI-1402978 and CMMI-1652575 is gratefully acknowledged. Any opinions, findings, and conclusions or recommendations expressed in this material are those of the authors and do not necessarily reflect the views of the National Science Foundation. The CW-LPBF samples were fabricated at Penn State's Center for Innovative Materials Processing through Direct Digital Deposition (CIMP-3D). The P-LPBF samples parts were made at Moog's Additive Manufacturing Center in East Aurora, NY. The authors thank Catherine Pomorski, Timothy Bowen, Divyesh Patel and Timothy Smith for their help in microstructural quantification.

References

[1] A.M. Beese, B.E. Carroll, Review of mechanical properties of Ti-6Al-4V made by laser-based additive manufacturing using powder feedstock, J. Miner. Metals Mater. Soc. 68 (2016) 724–734, http://dx.doi.org/10.1007/s11837-015-1759-z.
[2] S.L. Campanelli, N. Contuzzi, A.D. Ludovico, F. Caiazzo, F. Cardaropoli, V. Sergi, Manufacturing and characterization of Ti6Al4V lattice components manufactured by selective laser melting, Materials 7 (2014) 4803–4822, http://dx.doi.org/10.3390/ma7064803.
[3] D.D. Gu, W. Meiners, K. Wissenbach, R. Poprawe, Laser additive manufacturing of metallic components: materials, processes and mechanisms, Int. Mater. Rev. 57 (2012) 133–164, http://dx.doi.org/10.1179/1743280411Y.0000000014.
[4] H.K. Rafi, N.V. Karthik, H. Gong, T.L. Starr, B.E. Stucker, Microstructures and mechanical properties of Ti6Al4V parts fabricated by selective laser melting and electron beam melting, J. Mater. Eng. Perform. 22 (2013) 3872–3883, http://dx.doi.org/10.1007/s11665-013-0658-0.
[5] L. Thijs, F. Verhaeghe, T. Craeghs, J. Van Humbeeck, J.-P. Kruth, A study of the microstructural evolution during selective laser melting of Ti–6Al–4V, Acta Mater. 58 (2010) 3303–3312, http://dx.doi.org/10.1016/j.actamat.2010.02.004.
[6] SLM Solutions Group AG, SLM Solutions. 〈https://slm-solutions.com/machines〉 (Accessed 21 Feb 2017), 2017.
[7] ReaLizer GmbH, ReaLizer SLM. 〈http://www.realizer.com/en/?Page_id=987〉 (Accessed 21 Feb 2017).
[8] Concept Laser GmbH, Metal 3D printers - Concept Laser. 〈https://www.concept-laser.de/en/products/machines.html〉 (Accessed 21 Feb 2017).
[9] EOS e-Manufacturing Solutions, Additive Manufacturing of metal parts. 〈https://www.eos.info/systems_solutions/metal〉 (Accessed 21 Feb 2017), 2017.
[10] Sisma Industry, Additive Manufacturing. 〈http://www.sisma.com/eng/industry/prodotti/additive-manufacturing/〉 (Accessed 21 Feb 2017).
[11] Matsuura Machinery Corporation, Lumex Series. 〈http://www.lumex-matsuura.com/english/〉 (Accessed 21 Feb 2017).
[12] Renishaw plc, Metal additive manufacturing systems. 〈http://www.renishaw.com/en/metal-additive-manufacturing-3d-printing-systems–37011〉 (Accessed 21 Feb 2017).
[13] Market Tech Inc., Overview of Modulated and Pulsed Diode Laser Systems. 〈http://www.markettechinc.net/pdf/Diode〉 Laser Application Note.pdf (Accessed 20 Feb 2017).
[14] A. Mertens, S. Reginster, H. Paydas, Q. Contrepois, T. Dormal, O. Lemaire,

J. Lecomte-Beckers, Mechanical properties of alloy Ti–6Al–4V and of stainless steel 316L processed by selective laser melting: influence of out-of-equilibrium microstructures, Powder Metall. 57 (2014) 184–189, http://dx.doi.org/10.1179/1743290114Y.0000000092.
[15] P. Edwards, M. Ramulu, Fatigue performance evaluation of selective laser melted Ti–6Al–4V, Mater. Sci. Eng. A. 598 (2014) 327–337, http://dx.doi.org/10.1016/j.msea.2014.01.041.
[16] X. Zhao, S. Li, M. Zhang, Y. Liu, T.B. Sercombe, S. Wang, Y. Hao, R. Yang, L.E. Murr, Comparison of the microstructures and mechanical properties of Ti–6Al–4V fabricated by selective laser melting and electron beam melting, Mater. Des. 95 (2016) 21–31, http://dx.doi.org/10.1016/j.matdes.2015.12.135.
[17] M. Simonelli, Y.Y. Tse, C. Tuck, Effect of the build orientation on the mechanical properties and fracture modes of SLM Ti–6Al–4V, Mater. Sci. Eng. A 616 (2014) 1–11, http://dx.doi.org/10.1016/j.msea.2014.07.086.
[18] P. Åkerfeldt, M.-L. Antti, R. Pederson, Influence of microstructure on mechanical properties of laser metal wire-deposited Ti-6Al-4V, Mater. Sci. Eng. A 674 (2016) 428–437, http://dx.doi.org/10.1016/j.msea.2016.07.038.
[19] B.E. Carroll, T.A. Palmer, A.M. Beese, Anisotropic tensile behavior of Ti–6Al–4V components fabricated with directed energy deposition additive manufacturing, Acta Mater. 87 (2015) 309–320, http://dx.doi.org/10.1016/j.actamat.2014.12.054.
[20] C. Qiu, N.J.E. Adkins, M.M. Attallah, Microstructure and tensile properties of selectively laser-melted and of HIPed laser-melted Ti–6Al–4V, Mater. Sci. Eng. A 578 (2013) 230–239, http://dx.doi.org/10.1016/j.msea.2013.04.099.
[21] P. Edwards, A. O'Conner, M. Ramulu, Electron beam additive manufacturing of titanium components: properties and performance, J. Manuf. Sci. Eng. 135 (2013) 61016, http://dx.doi.org/10.1115/1.4025773.
[22] T. Vilaro, C. Colin, J.D. Bartout, As-fabricated and heat-treated microstructures of the Ti-6Al-4V alloy processed by selective laser melting, Metall. Mater. Trans. A 42 (2011) 3190–3199, http://dx.doi.org/10.1007/s11661-011-0731-y.
[23] M. Shunmugavel, A. Polishetty, G. Littlefair, Microstructure and mechanical properties of wrought and additive manufactured Ti-6Al-4V cylindrical bars, Proc. Technol. 20 (2015) 231–236, http://dx.doi.org/10.1016/j.protcy.2015.07.037.
[24] ASTM Int., Standard Test Methods for Tension Testing of Metallic Materials, ASTM Int'l. ASTM E8, 2009, pp. 1–27, http://dx.doi.org/10.1520/E0008.
[25] J.A. Slotwinski, E.J. Garboczi, K.M. Hebenstreit, Porosity measurements and analysis for metal additive manufacturing process control, J. Res. Natl. Inst. Stand. Technol. 119 (2014) 494–528, http://dx.doi.org/10.6028/jres.119.019.
[26] G. Ziółkowski, E. Chlebus, P. Szymczyk, J. Kurzac, Application of X-ray CT method for discontinuity and porosity detection in 316L stainless steel parts produced with SLM technology, Arch. Civ. Mech. Eng. 14 (2014) 608–614, http://dx.doi.org/10.1016/j.acme.2014.02.003.
[27] M.J. Donachie, Titanium: A Technical Guide, 2nd ed, ASM International, Materials ParkMaterials Park, OH, 2000.
[28] Y. Sato, M. Tsukamoto, Y. Yamashita, Surface morphology of Ti–6Al–4V plate fabricated by vacuum selective laser melting, Appl. Phys. B. 119 (2015) 545–549, http://dx.doi.org/10.1007/s00340-015-6059-3.
[29] S. Soares da Rocha, G. Luis Adabo, G. Elias Pessanha Henriques, M. Antônio de Arruda Nobilo, G. Luis Adabo, Vickers hardness of cast commercially pure titanium and Ti-6Al-4V alloy submitted to heat treatments, Braz. Dent. J. 17 (2006), 〈http://www.scielo.br/pdf/bdj/v17n2/v17n2a08.pdf〉 (accessed 7 December 2016).
[30] R.K. Gupta, C. Mathew, P. Ramkumar, Strain hardening in aerospace alloys, Front. Aerosp. Eng. 4 (2015) 1–13, http://dx.doi.org/10.12783/fae.2015.0401.01.
[31] J.H. Hollomon, Tensile deformation, Trans. Metall. Soc. AIME 162 (1945) 268–290.
[32] C. Qiu, G.A. Ravi, C. Dance, A. Ranson, S. Dilworth, M.M. Attallah, Fabrication of large Ti–6Al–4V structures by direct laser deposition, J. Alloy. Compd. 629 (2015) 351–361, http://dx.doi.org/10.1016/j.jallcom.2014.12.234.
[33] H.K. Rafi, T.L. Starr, B.E. Stucker, A comparison of the tensile, fatigue, and fracture behavior of Ti–6Al–4V and 15-5 PH stainless steel parts made by selective laser melting, Int. J. Adv. Manuf. Technol. 69 (2013) 1299–1309, http://dx.doi.org/10.1007/s00170-013-5106-7.
[34] S. Palanivel, A.K. Dutt, E.J. Faierson, R.S. Mishra, Spatially dependent properties in a laser additive manufactured Ti–6Al–4V component, Mater. Sci. Eng. A 654 (2016) 39–52, http://dx.doi.org/10.1016/j.msea.2015.12.021.
[35] H. Galarraga, D.A. Lados, R.R. Dehoff, M.M. Kirka, P. Nandwana, Effects of the microstructure and porosity on properties of Ti-6Al-4V ELI alloy fabricated by electron beam melting (EBM), Addit. Manuf. 10 (2016) 47–57, http://dx.doi.org/10.1016/j.addma.2016.02.003.
[36] S. Kou, Welding Metallurgy, 2nd ed, John Wiley & Sons, Inc, Hoboken, NJ, 2003.
[37] Y. Li, D. Gu, Parametric analysis of thermal behavior during selective laser melting additive manufacturing of aluminum alloy powder, Mater. Des. 63 (2014) 856–867, http://dx.doi.org/10.1016/j.matdes.2014.07.006.
[38] T. Mukherjee, V. Manvatkar, A. De, T. DebRoy, Dimensionless numbers in additive manufacturing, J. Appl. Phys. 121 (2017) 64904, http://dx.doi.org/10.1063/1.4976006.
[39] P.A. Kobryn, S.L. Semiatin, Microstructure and texture evolution during solidification processing of Ti–6Al–4V, J. Mater. Process. Technol. 135 (2003) 330–339, http://dx.doi.org/10.1016/S0924-0136(02)00865-8.
[40] V. Manvatkar, A. De, T. DebRoy, Spatial variation of melt pool geometry, peak temperature and solidification parameters during laser assisted additive manufacturing process, Mater. Sci. Technol. 31 (2015) 924–930, http://dx.doi.org/10.1179/1743284714Y.0000000701.
[41] X. He, P.W. Fuerschbach, T. DebRoy, Heat transfer and fluid flow during laser spot welding of 304 stainless steel, J. Phys. D Appl. Phys. 36 (2003) 1388–1398, http://dx.doi.org/10.1088/0022-3727/36/12/306.
[42] R. Chou, A. Ghosh, S.C. Chou, M. Paliwal, M. Brochu, Microstructure and mechanical properties of Al10SiMg fabricated by pulsed laser powder bed fusion, Mater. Sci. Eng. A 689 (2017) 53–62, http://dx.doi.org/10.1016/j.msea.2017.02.023.
[43] G.J. Marshall, W.J. Young, S.M. Thompson, N. Shamsaei, S.R. Daniewicz, S. Shao, Understanding the microstructure formation of Ti-6Al-4V during direct laser deposition via in-situ thermal monitoring, J. Miner. Metals mater. Soc. 68 (2016) 778–790, http://dx.doi.org/10.1007/s11837-015-1767-z.
[44] G. Lütjering, J.C. Williams, Titanium: engineering materials and processes, Second (2007), http://dx.doi.org/10.1007/978-3-540-73036-1.
[45] D. Greitemeier, F. Palm, F. Syassen, T. Melz, Fatigue performance of additive manufactured TiAl6V4 using electron and laser beam melting, Int. J. Fatigue (2016), http://dx.doi.org/10.1016/j.ijfatigue.2016.05.001.
[46] E. Wycisk, C. Emmelmann, S. Siddique, F. Walther, High cycle fatigue (HCF) performance of Ti-6Al-4V alloy processed by selective laser melting, Adv. Mater. Res. 816–817 (2013) 134–139, http://dx.doi.org/10.4028/www.scientific.net/AMR.816-817.134.
[47] J.S. Keist, T.A. Palmer, Role of geometry on properties of additively manufactured Ti-6Al-4V structures fabricated using laser based directed energy deposition, Mater. Des. 106 (2016) 482–494, http://dx.doi.org/10.1016/j.matdes.2016.05.045.
[48] E. Oberg, F.D. Jones, H.L. Horton, H.H. Ryffel, Machinery's Handbook, 28th ed, Industrial Press, Inc., New York, 2008.